Computer Assisted Methods in Engineering and Science, **20**: 337–348, 2013.

TWENTY YEARS OF THE CAMES

On inverse form finding for orthotropic plasticity

Philipp Landkammer, Sandrine Germain, Paul Steinmann
Chair of Applied Mechanics, University Erlangen-Nuremberg
Egerlandstrasse 5, 91058 Erlangen, Germany
e-mails: philipp.landkammer@ltm.uni-erlangen.de,
sandrine.germain@ltm.uni-erlangen.de, paul.steinmann@ltm.uni-erlangen.de

Inverse form finding aims to determine the optimum blank design of a workpiece whereby the desired spatial configuration that is obtained after a forming process, the boundary conditions and the applied loads are known. Inputting the optimal material configuration, a subsequent FEM computation then has to result exactly in the nodal coordinates of the desired deformed workpiece. Germain et al. [1] recently presented a new form finding strategy for isotropic elastoplasticity. Switching between the direct and the inverse mechanical formulation, while fixing the internal plastic variables in the inverse step, uniquely detects the undeformed configuration iteratively. In this contribution, the developed recursive algorithm is extended to anisotropic plasticity. In particular the orthotropic Hill yield function is considered. A load and a displacement-controlled example demonstrate that this new strategy requires only a few iterations to determine the optimal initial design whereby an almost linear convergence rate is obtained.

Keywords: inverse FEM, inverse form finding, orthotropic Hill's yield criterion, logarithmic strain space, optimum blank design.

1. Introduction

The overall goal of inverse form finding is to determine an optimum blank design for forming processes. Consequently, time and costs could be saved during development process of functional components. The scope of this work is finding a proper undeformed material configuration to a desired deformed shape of a workpiece. This is illustrated in Fig. 1.

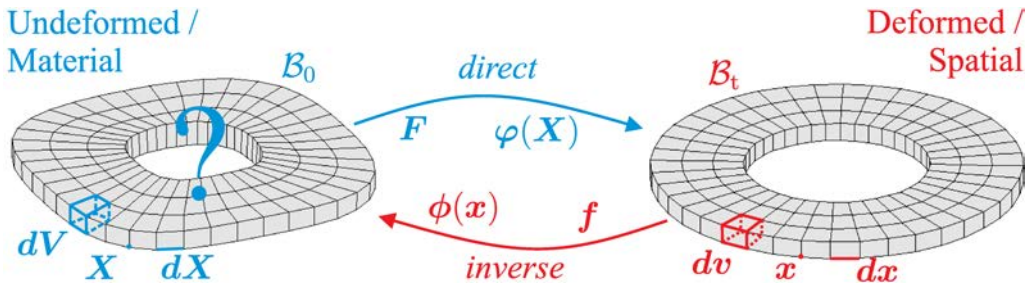

Fig. 1. Inverse form finding: the material configuration $\mathcal{B}_0$ is sought while the desired spatial configuration $\mathcal{B}_t$ is given; illustration of the direct (blue) and inverse (red) mechanical formulation.

Recalculating the (direct) forming simulation, by inputting the optimal material node positions, results exactly in the desired nodal coordinates of the spatial configuration. To describe the problem of inverse form finding in analytical way, an objective function $\delta(\boldsymbol{X})$ is used as in [2], see Eq. (1). The solution is found, if the squared summed differences between the currently computed node positions $\boldsymbol{x}_{\text{current}}$ and the given desired node positions $\boldsymbol{x}_{\text{target}}$ are less than a certain tolerance limit.

The objective function $\delta(\boldsymbol{X})$ has to be minimized with respect to the nodal coordinates $\boldsymbol{X}$ of the undeformed workpiece, whereas the corresponding direct FEM simulation serves as a state equation

$$\min_{\boldsymbol{X}} \delta(\boldsymbol{X}) = \|\boldsymbol{x}_{\text{target}} - \boldsymbol{x}_{\text{current}}(\boldsymbol{X})\|^2. \tag{1}$$

There exist different approaches to solve the minimization problem, in particular, various methods from sensitivity analysis, e.g., [2] and [3]. Gradient-based approaches often suffer from high computational costs as well as from mesh distortions, see [4] and [5]. On the contrary, the algorithm presented in Germain et al. [1] works in a totally different way. This new approach is based on an inverse finite element method, which formulates the mechanical weak form in the spatial configuration $\mathcal{B}_{\text{t}}$ and solves it with respect to the coordinates in the material configuration $\mathcal{B}_0$.

The inverse mechanical formulation was first proposed by Govindjee and Mihalic [6] for neo-Hookean type materials. In the last two decades the inverse computation was applied to a wide range of problems. Govindjee and Mihalic [7], for example, extended the method also to temperature changes and orthotropic nonlinear elasticity, while using a Saint Venant type material.

Germain and Steinmann [8] showed that the inverse approach also works for anisotropic hyperelasticity in the logarithmic strain space. Furthermore, in [9] the efficiency of the inverse FEM in comparison to a gradient-based sensitivity analysis in an example of stamping of a hyperelastic sheet was demonstrated. Ask et al. [10] recently presented an inverse formulation within the application to electroelasticity.

Concerning inverse form finding problems in metal forming, Germain and Steinmann [11] applied this approach to elastoplasticity, in particular, to a cubic elastic material behavior in addition to the isotropic von Mises yield criterion. Thereby, an inverse FEM simulation recalculated exactly the material configuration, when the spatial configuration, the plastic strains and the hardening parameters were known. The drawback for calculating a unique undeformed material configuration is that the internal (plastic) variables are in general not previously given at each Gauss point. Recently, Germain et al. [1] presented a recursive algorithm to circumvent this drawback with application to isotropic plasticity. While using the inverse formulation in addition to the direct solution in the sense of a fixed-point iteration, the material configuration is updated iteratively until an admissible solution is found.

In this contribution, the work of [1] is extended to the anisotropic Hill yield function. The Hill yield criterion is frequently used in metal forming, since rolled sheets have a different yield stress in and perpendicular to the rolling direction. In order to approximate contact problems, it is shown in this paper that the new strategy also works for displacement controlled problems.

The paper is structured as follows: Sec. 2 describes the numerical background for the material behavior and the mechanical formulation. The stress-strain relationships in the logarithmic strain space, utilized to capture large inelastic deformations, are characterized in Subsec. 2.1. The integration algorithm employed to model the orthotropic Hill plasticity is presented in Subsec. 2.2. The different mechanical formulations, as the basic elements of the form finding algorithm, are explained in detail in Subsec. 2.3. The corresponding algorithm to solve the form finding problem is shown in Sec. 3. Two examples under load and displacement control are provided in Sec. 4 to demonstrate the capability of the advocated algorithm. Finally, Sec. 5 concludes the work.

2. Computational material modeling

2.1. Logarithmic strain space formulation for large inelastic deformations

To capture large inelastic deformations as occurring in metal forming applications, a transformation to the logarithmic strain space was proposed by Miehe et al. [12] and Apel [13] in terms of a three-step approach.

The preprocessing into the logarithmic strain space is performed based on the spectral decomposition of the right Cauchy-Green tensor $\boldsymbol{C}$ as defined in [14]. Due to its symmetry property, the

Cauchy-Green tensor $\boldsymbol{C}$ can be decomposed into its eigenvalues $\lambda_{\mathrm{i}} \in \mathbb{R}$ $(\mathrm{i} = 1, 2, 3)$ and eigenbases $\boldsymbol{M}_{\mathrm{i}} \in \mathbb{R}^{3\times 3}$ $(\mathrm{i} = 1, 2, 3)$, as proposed in, e.g., [11] and [15]. Correspondingly, the logarithmic strains read

$$\boldsymbol{E} = \frac{1}{2}\ln(\boldsymbol{C}) = \frac{1}{2}\ln(\boldsymbol{F}^{\top} \cdot \boldsymbol{F}) = \frac{1}{2}\sum_{\mathrm{i}=1}^{3} \ln(\lambda_{\mathrm{i}})\boldsymbol{M}_{\mathrm{i}}. \tag{2}$$

Thus, the obtained logarithmic strain tensor corresponds to the Hencky strain tensor, which is widely used in the metal forming context. As proposed in [12] an additive decomposition of the logarithmic strain tensor $\boldsymbol{E}$ into an elastic and a plastic part is assumed. Thus, the additive structure for the strains as postulated in the geometrically linear theory is assumed.

$$\boldsymbol{E}^{\mathrm{e}} = \boldsymbol{E} - \boldsymbol{E}^{\mathrm{p}}. \tag{3}$$

From their counterparts $\boldsymbol{T}$ and $\mathbb{E}^{\mathrm{ep}}$ in the logarithmic space a postprocessing step is required to obtain the 2nd Piola-Kirchhoff stress $\boldsymbol{S}$ and the corresponding elastoplastic tangent $\mathbb{C}^{\mathrm{ep}}$. This transformation from the logarithmic space is accomplished by the following relations:

$$\boldsymbol{S} = \boldsymbol{T} : \mathbb{P} \qquad \text{and} \qquad \mathbb{C}^{\mathrm{ep}} = \mathbb{P}^{\top} : \mathbb{E}^{\mathrm{ep}} : \mathbb{P} + \boldsymbol{T} : \mathbb{L}. \tag{4}$$

More details on the calculation of the transformation tensors $\mathbb{P} = 2\dfrac{\partial \boldsymbol{E}}{\partial \boldsymbol{C}}$ and $\mathbb{L} = 4\dfrac{\partial^2 \boldsymbol{E}}{\partial \boldsymbol{C}\partial \boldsymbol{C}}$ can be found in [14] and [12].

Table 1. Geometrically nonlinear orthotropic Hill-type elastoplasticity in a nutshell

Input / Preprocessing	
log. strain tensor	$\boldsymbol{E} = \frac{1}{2}\ln(\boldsymbol{C}) = \frac{1}{2}\ln(\boldsymbol{F}^{\top} \cdot \boldsymbol{F})$
Constitutive modeling in the log. strain space	
add. decomposition	$\boldsymbol{E}^{\mathrm{e}} = \boldsymbol{E} - \boldsymbol{E}^{\mathrm{p}}$
energy storage function	$\Psi(\boldsymbol{E}^{\mathrm{e}}, \alpha) = \Psi^{\mathrm{e}}(\boldsymbol{E}^{\mathrm{e}}) + \Psi^{\mathrm{p}}(\alpha)$
stress tensor	$\boldsymbol{T} = \partial_{\boldsymbol{E}^{\mathrm{e}}}\Psi^{\mathrm{e}}(\boldsymbol{E}^{\mathrm{e}}) = \mathbb{E} : \boldsymbol{E}^{\mathrm{e}}$
yield stress	$y(\alpha) = -\partial_{\alpha}\Psi^{\mathrm{p}}(\alpha)$
(Hill) yield function	$\Phi(\boldsymbol{T}, \alpha) = \|\boldsymbol{T}\|_{\mathbb{H}} - \sqrt{\frac{2}{3}}y(\alpha)$
flow rule	$\dot{\boldsymbol{E}}^{\mathrm{p}} = \lambda\partial_{\boldsymbol{T}}\Phi = \lambda\dfrac{\mathbb{H} : \boldsymbol{T}}{\|\boldsymbol{T}\|_{\mathbb{H}}}$
evolution equation	$\dot{\alpha} = \lambda\partial_{y}\Phi = \lambda\sqrt{\frac{2}{3}}$
Output in the log. strain space	
stress tensor	$\boldsymbol{T}$
tangent tensor	$\mathbb{E}^{\mathrm{ep}} = \dfrac{\partial \boldsymbol{T}}{\partial \boldsymbol{E}}$
internal plastic variables	$\{\boldsymbol{E}^{\mathrm{p}}, \alpha\}$
Postprocessing	
2nd P.-K. stress tensor	$\boldsymbol{S} = \boldsymbol{T} : \mathbb{P}$
tangent tensor	$\mathbb{C}^{\mathrm{ep}} = \dfrac{\partial \boldsymbol{S}}{\partial \boldsymbol{C}} = \mathbb{P}^{\top} : \mathbb{E}^{\mathrm{ep}} : \mathbb{P} + \boldsymbol{T} : \mathbb{L}$

References [12] and [16] additionally demonstrated that the results obtained by an additive framework of plasticity in the logarithmic space are close to those obtained by the common multiplicative decomposition even in the case of non-coaxial deformations. A further strong argument for the use of additive plasticity in the logarithmic space is the much simpler structure compared to that of multiplicative plasticity, see Miehe et al. [12]. The basic equations of the used constitutive model are listed in Table 1.

2.2. Integration algorithm for the orthotropic Hill yield criterion

As the prototype of anisotropic plasticity, the quadratic orthotropic Hill yield criterion, see Hill [17],

$$\Phi(\boldsymbol{T}, \alpha) = \|\boldsymbol{T}\|_{\mathbb{H}} - \sqrt{\frac{2}{3}} y(\alpha), \tag{5}$$

whereby

$$\|\boldsymbol{T}\|_{\mathbb{H}} = \sqrt{\boldsymbol{T}^{\top} : \mathbb{H} : \boldsymbol{T}} \tag{6}$$

is used in the subsequent examples in Sec. 4.

The Hill-tensor $\mathbb{H}$ is defined in Voigt's notation by Eq. (7), whereby the diagonal entries are defined in Eq. (8). These entries describe the ratio of the reference yield stress y_0 to the yield stress $y_{\mathrm{ij}} \in \mathbb{R}$ $(\mathrm{i}, \mathrm{j} = 1, 2, 3)$ for each direction. The non-diagonal entries are given by Eq. (9). Furthermore, by setting all coefficients $\alpha_{\mathrm{i}} \in \mathbb{R}$ $(\mathrm{i} = 1, 2, \ldots, 9)$ equal to 1, the Hill yield criterion reduces to the isotropic von Mises yield criterion.

$$\mathbb{H} = \begin{bmatrix} \alpha_1 & \frac{1}{2}\alpha_4 & \frac{1}{2}\alpha_6 & 0 & 0 & 0 \\ \frac{1}{2}\alpha_4 & \alpha_2 & \frac{1}{2}\alpha_5 & 0 & 0 & 0 \\ \frac{1}{2}\alpha_6 & \frac{1}{2}\alpha_5 & \alpha_2 & 0 & 0 & 0 \\ 0 & 0 & 0 & \frac{1}{2}\alpha_7 & 0 & 0 \\ 0 & 0 & 0 & 0 & \frac{1}{2}\alpha_8 & 0 \\ 0 & 0 & 0 & 0 & 0 & \frac{1}{2}\alpha_9 \end{bmatrix}, \tag{7}$$

$$\begin{aligned} &\alpha_1 = \frac{2}{3}\frac{y_0^2}{y_{11}^2}, \qquad \alpha_2 = \frac{2}{3}\frac{y_0^2}{y_{22}^2}, \qquad \alpha_3 = \frac{2}{3}\frac{y_0^2}{y_{33}^2}, \\ &\alpha_7 = \frac{1}{3}\frac{y_0^2}{y_{12}^2}, \qquad \alpha_8 = \frac{2}{3}\frac{y_0^2}{y_{23}^2}, \qquad \alpha_9 = \frac{2}{3}\frac{y_0^2}{y_{13}^2}, \end{aligned} \tag{8}$$

$$\begin{aligned} &\alpha_4 = \alpha_3 - \alpha_1 - \alpha_2, \\ &\alpha_5 = \alpha_1 - \alpha_2 - \alpha_3, \\ &\alpha_6 = \alpha_2 - \alpha_1 - \alpha_3. \end{aligned} \tag{9}$$

To integrate the elastoplastic rate equations a fully implicit Euler backward method is taken into account, in which the gradient to the yield function is evaluated at the end of each loading step. When dealing with the orthotropic Hill yield function, the Newton algorithm for finding the

appropriate plastic multiplier increment $\lambda \in \mathbb{R}$ must be able to capture the changing flow direction in each Newton step:

$$\boldsymbol{N}(\boldsymbol{T}) = \frac{\mathbb{H} : \boldsymbol{T}}{\|\boldsymbol{T}\|_{\mathbb{H}}}. \tag{10}$$

The integration algorithm, proposed by de Borst and Feenstra [18] for the geometrically linear and anisotropic quadratic Hill criterion, is here applied to the constitutive model in the logarithmic space, see Subsec. 2.1. The current logarithmic stress tensor $\boldsymbol{T}$ is expressed dependent on the trial stress $\boldsymbol{T}^*$ as

$$\boldsymbol{T}(\lambda, \boldsymbol{T}^*) = \boldsymbol{T}^* - \lambda \mathbb{E} : \boldsymbol{N}\big(\boldsymbol{T}(\lambda)\big). \tag{11}$$

With the requirement

$$\Phi(\boldsymbol{T}, \alpha) = 0 \tag{12}$$

one obtains

$$\boldsymbol{T}(\lambda, \boldsymbol{T}^*) = \Big[\boldsymbol{I}_{\mathrm{sym}} + \lambda \frac{1}{\sqrt{\frac{2}{3}} y(\alpha)} \mathbb{E} : \mathbb{H}\Big]^{-1} : \boldsymbol{T}^* = \mathbb{A}(\lambda)^{-1} : \boldsymbol{T}^*. \tag{13}$$

Inserting Eq. (13) into Eq. (12) leads to

$$\Phi(\lambda, \boldsymbol{T}^*, \alpha) = \|\mathbb{A}^{-1} : \boldsymbol{T}^*\|_{\mathbb{H}} - \sqrt{\frac{2}{3}} y(\alpha) = 0. \tag{14}$$

This equation can then be solved for λ with the Newton method. The corresponding derivative of the residual Eq. (14) reads as

$$\partial_\lambda \Phi = \frac{\boldsymbol{T}^{*\top} : [\mathbb{B}^\top + \mathbb{B}] : \boldsymbol{T}^*}{2\sqrt{\frac{2}{3}} y(\alpha) \|\mathbb{A}^{-1} : \boldsymbol{T}^*\|_{\mathbb{H}}} \tag{15}$$

whereby

$$\mathbb{B} = \mathbb{E} : \mathbb{H} : \mathbb{A}^{-2} : \mathbb{H} : \mathbb{A}^{-1}. \tag{16}$$

Applying this integration algorithm to the orthotropic Hill yield function, a quadratic rate of convergence for computing the plastic multiplier increment λ can be obtained. The elastoplastic tangent

$$\mathbb{E}^{\mathrm{ep}} = \frac{\partial \boldsymbol{T}}{\partial \boldsymbol{E}} = \mathbb{E}^{\#} - \frac{[\mathbb{E}^{\#} : \boldsymbol{N}] \otimes [\mathbb{E}^{\#} : \boldsymbol{N}]}{\boldsymbol{N} : \mathbb{E}^{\#} : \boldsymbol{N} + \frac{2}{3} y(\alpha)} \tag{17}$$

whereby

$$\mathbb{E}^{\#} = \Big[\mathbb{E}^{-1} + \frac{\lambda}{\|\boldsymbol{T}\|_{\mathbb{H}}} [\mathbb{H} - \boldsymbol{N} \otimes \boldsymbol{N}]\Big]^{-1}, \tag{18}$$

consistent with the Euler backward integration method, is then utilized for the linearization of the stress-strain relationship in the approach based on logarithmic strain measures. The elastoplastic tangent $\mathbb{C}^{\mathrm{ep}}$ in the total strain space is finally provided by the postprocessing step, see Eq. (4) and Table 1.

2.3. The direct and inverse mechanical formulation

As illustrated in Fig. 1, FE analysis can be performed either starting at the material configuration $\mathcal{B}_0$ parameterized in $\boldsymbol{X}$ or at the spatial configuration $\mathcal{B}_\mathrm{t}$ parameterized in $\boldsymbol{x}$. This was exploited, e.g., in [6–8] to solve the inverse form finding problem.

Considering the usual direct FEM, the boundary value problem (BVP) is formulated in the material configuration $\mathcal{B}_0$. The goal is to determine the deformation map $\boldsymbol{\varphi}(\boldsymbol{X})$ to obtain the spatial coordinates $\boldsymbol{x}$ of the spatial configuration $\mathcal{B}_\mathrm{t}$. The deformation gradient $\boldsymbol{F} = \nabla\boldsymbol{\varphi}(\boldsymbol{X})$ leads to the logarithmic strain tensor $\boldsymbol{E}$ as in [11], see Eq. (2). The equilibrium equation in this case depends on the 1st Piola-Kirchhoff stress $\boldsymbol{P} = \boldsymbol{F} \cdot \boldsymbol{S}$ as proposed in [8]. As also denoted in [8], the weak form employs test functions $\boldsymbol{\eta} \in \mathcal{V}_0 = \{\boldsymbol{\eta} | \boldsymbol{\eta} = 0 \text{ on } \partial\mathcal{B}_0^{\overline{\boldsymbol{\varphi}}}\}$ according to the boundary conditions (BC) of the material configuration $\mathcal{B}_0$. To solve the weak form of equilibrium via the Newton-Raphson method, its linearization, as depicted in Table 2, is required. Therein, the total elastoplastic tangent $\mathbb{C}^{\mathrm{ep}}$ from the relationship $\dfrac{\partial \boldsymbol{P}}{\partial \boldsymbol{F}}$, see Table 2, is obtained by the postprocessing of the three-step approach, see Eq. (4).

Table 2. The direct mechanical formulation at fixed material coordinates $\boldsymbol{X}$ [19].

BVP in the material configuration $\mathcal{B}_0$

Equilibrium equation	$\mathrm{Div}\boldsymbol{P} = 0$	on $\mathcal{B}_0$
stress BC	$\boldsymbol{P} \cdot \overline{\boldsymbol{N}} = \overline{\boldsymbol{T}}$	on $\partial\mathcal{B}_0^{\overline{\boldsymbol{T}}}$
displacement BC	$\boldsymbol{\varphi} = \overline{\boldsymbol{\varphi}}$	on $\mathcal{B}_0^{\overline{\boldsymbol{\varphi}}}$

Weak formulation of equilibrium

$$G(\boldsymbol{\varphi}, \boldsymbol{\eta}; \boldsymbol{X}) = \int_{\mathcal{B}_0} \boldsymbol{\eta} \cdot \mathrm{Div}\boldsymbol{P} dV = \int_{\partial\mathcal{B}_0^{\overline{\boldsymbol{T}}}} \boldsymbol{\eta} \cdot \overline{\boldsymbol{T}} dA - \int_{\mathcal{B}_0} \mathrm{Grad}\boldsymbol{\eta} : \boldsymbol{P} dV = 0 \quad \forall\, \boldsymbol{\eta} \in \mathcal{V}_0$$

Linearization for Newton-Raphson method

$$\mathcal{D}_{\boldsymbol{\varphi}} G(\boldsymbol{\varphi}, \boldsymbol{\eta}; \boldsymbol{X}) = \frac{\mathrm{d}}{\mathrm{d}\varepsilon} G(\boldsymbol{\varphi} + \varepsilon\Delta\boldsymbol{\varphi}, \boldsymbol{\eta}; \boldsymbol{X})\big|_{\varepsilon=0} =$$

$$= \int_{\mathcal{B}_0} \mathrm{Grad}\boldsymbol{\eta} : \frac{\partial \boldsymbol{P}}{\partial \boldsymbol{F}} : \frac{\mathrm{d}}{\mathrm{d}\varepsilon} \boldsymbol{F}(\boldsymbol{\varphi} + \varepsilon\Delta\boldsymbol{\varphi}, \boldsymbol{\eta}; \boldsymbol{X})\big|_{\varepsilon=0} dV = \int_{\mathcal{B}_0} \mathrm{Grad}\boldsymbol{\eta} : \frac{\partial \boldsymbol{P}}{\partial \boldsymbol{F}} : \mathrm{Grad}\Delta\boldsymbol{\varphi} dV \quad \forall\, \boldsymbol{\eta} \in \mathcal{V}_0$$

whereby $\dfrac{\partial \boldsymbol{P}}{\partial \boldsymbol{F}} = [\boldsymbol{F} \overline{\otimes} \boldsymbol{I}] : \mathbb{C}^{\mathrm{ep}} : [\boldsymbol{F}^{\top} \overline{\otimes} \boldsymbol{I}] + \boldsymbol{I} \overline{\otimes} \boldsymbol{S}$

and $\overline{\otimes}$ a non-standard dyadic product: $[\boldsymbol{A} \overline{\otimes} \boldsymbol{B}]_{ijkl} = \boldsymbol{A}_{ik}\boldsymbol{B}_{jl}$

On the contrary, within the inverse type of the FEM, the mechanical problem is formulated in the spatial configuration $\mathcal{B}_\mathrm{t}$, as in [6]. The Cauchy stress $\boldsymbol{\sigma}$ is obtained by a push forward from the 2nd Piola-Kirchhoff stress $\boldsymbol{S}$ as proposed in [11]. The weak form employs test functions $\boldsymbol{\eta} \in \mathcal{V}_\mathrm{t} = \{\boldsymbol{\eta} | \boldsymbol{\eta} = 0 \text{ on } \partial\mathcal{B}_\mathrm{t}^{\overline{\boldsymbol{\phi}}}\}$ according to the boundary conditions of the spatial configuration $\mathcal{B}_\mathrm{t}$. Determination of the inverse deformation map $\boldsymbol{\phi}(\boldsymbol{x}) = \boldsymbol{\varphi}^{-1}$ results in the material coordinates $\boldsymbol{X}$ of the material configuration $\mathcal{B}_0$, which can also be found in [11]. The deformation gradient $\boldsymbol{f} = \nabla\boldsymbol{\phi}(\boldsymbol{x})$ is again utilized to compute the logarithmic strain tensor $\boldsymbol{E}$. In Table 3 the inverse mechanical formulation and the linearization of the weak form for applying the Newton-Raphson method are depicted. The elastoplastic tangent $\mathbb{C}^{\mathrm{ep}}$ from the relationship $\dfrac{\partial \boldsymbol{\sigma}}{\partial \boldsymbol{f}}$ is obtained by the postprocessing of the three-step approach as in the direct formulation. A detailed description of the direct and the inverse mechanical formulation in the logarithmic strain space can be found in Germain [19].

Table 3. The inverse mechanical formulation at fixed spatial coordinates $\boldsymbol{x}$ [19].

BVP in the spatial configuration $\mathcal{B}_\mathrm{t}$

Equilibrium equation	$\mathrm{div}\boldsymbol{\sigma} = 0$	on $\mathcal{B}_\mathrm{t}$
stress BC	$\boldsymbol{\sigma}\cdot\overline{\boldsymbol{n}} = \overline{\boldsymbol{t}}$	on $\partial\mathcal{B}_\mathrm{t}^{\overline{t}}$
displacement BC	$\boldsymbol{\phi} = \overline{\boldsymbol{\phi}}$	on $\partial\mathcal{B}_\mathrm{t}^{\overline{\phi}}$

Weak formulation of equilibrium

$$g(\boldsymbol{\phi},\boldsymbol{\eta};\boldsymbol{x}) = \int_{\mathcal{B}_\mathrm{t}} \boldsymbol{\eta}\cdot\mathrm{div}\boldsymbol{\sigma}\,dv = \int_{\partial\mathcal{B}_\mathrm{t}^{\overline{t}}} \boldsymbol{\eta}\cdot\overline{\boldsymbol{t}}\,da - \int_{\mathcal{B}_\mathrm{t}} \mathrm{grad}\boldsymbol{\eta} : \boldsymbol{\sigma}\,dv = 0 \quad \forall\ \boldsymbol{\eta}\in\mathcal{V}_\mathrm{t}$$

Linearization for Newton-Raphson method

$$\mathcal{D}_{\boldsymbol{\phi}} g(\boldsymbol{\phi},\boldsymbol{\eta};\boldsymbol{x}) = \frac{\mathrm{d}}{\mathrm{d}\varepsilon} g(\boldsymbol{\phi}+\varepsilon\Delta\boldsymbol{\phi},\boldsymbol{\eta};\boldsymbol{x})\big|_{\varepsilon=0} =$$

$$= \int_{\mathcal{B}_\mathrm{t}} \mathrm{grad}\boldsymbol{\eta} : \frac{\partial\boldsymbol{\sigma}}{\partial\boldsymbol{f}} : \frac{\mathrm{d}}{\mathrm{d}\varepsilon}\boldsymbol{f}(\boldsymbol{\phi}+\varepsilon\Delta\boldsymbol{\phi},\boldsymbol{\eta};\boldsymbol{x})\big|_{\varepsilon=0} dv = \int_{\mathcal{B}_\mathrm{t}} \mathrm{grad}\boldsymbol{\eta} : \frac{\partial\boldsymbol{\sigma}}{\partial\boldsymbol{f}} : \mathrm{grad}\Delta\boldsymbol{\phi}\,dv \quad \forall\ \boldsymbol{\eta}\in\mathcal{V}_0$$

whereby $\dfrac{\partial\boldsymbol{\sigma}}{\partial\boldsymbol{f}} = \boldsymbol{\sigma}\otimes\boldsymbol{F}^\top - \boldsymbol{F}\overline{\otimes}\boldsymbol{\sigma} + \boldsymbol{j}\boldsymbol{F}\cdot\left[\dfrac{1}{2}\mathbb{C}^\mathrm{ep} : \dfrac{\partial\boldsymbol{C}}{\partial\boldsymbol{f}}\right]\cdot\boldsymbol{F}^\top - \boldsymbol{\sigma}\underline{\otimes}\boldsymbol{F}$

$\overline{\otimes}$ and $\underline{\otimes}$ non-standard dyadic products: $[\boldsymbol{A}\overline{\otimes}\boldsymbol{B}]_{ijkl} = \boldsymbol{A}_{ik}\boldsymbol{B}_{jl}$ and $[\boldsymbol{A}\underline{\otimes}\boldsymbol{B}]_{ijkl} = \boldsymbol{A}_{il}\boldsymbol{B}_{jk}$

Although the inverse approach is based on a different kinematic description, nearly all subroutines of an existing FEM code can be reused, even the pre- and post-processor of the three-step approach to the logarithmic strain space and the integration algorithm for plasticity. The numerical costs and therefore the time for computations are also comparable to each other. Combining the three-step approach, the integration algorithm for plasticity and the consistent tangent matrix $\mathbb{C}^\mathrm{ep}$, a global quadratic convergence rate in the direct and inverse computations is achieved.

3. Form finding algorithm

The procedure of the advocated algorithm is in accordance with the algorithm proposed by Germain et al. [1] for isotropic plasticity. For the purpose of better understanding, Fig. 2 illustrates the form finding strategy graphically.

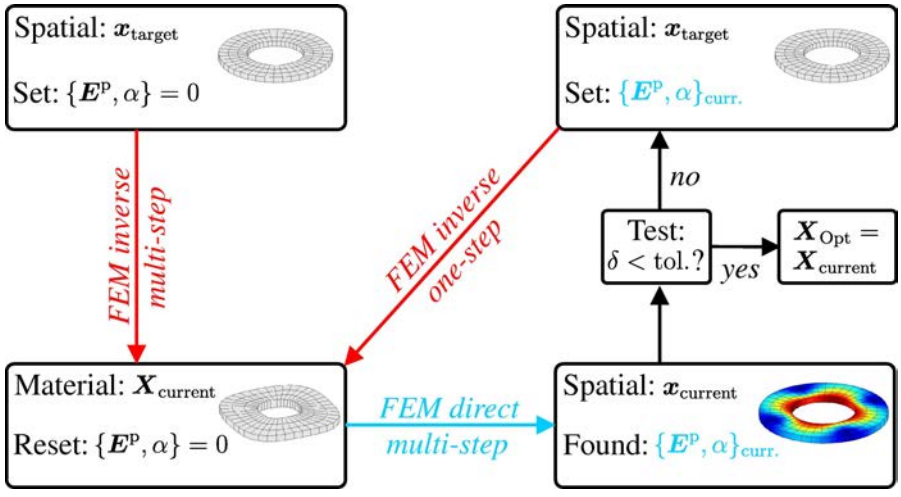

Fig. 2. A sketch of the recursive form finding algorithm as proposed in [1].

The algorithm to determine the optimum blank design starts with the desired spatial configuration $\mathcal{B}_\mathrm{t}$, whereby $\boldsymbol{x}_\mathrm{target}$ are the given node positions of the desired deformed shape of the workpiece. FEM computation based on the inverse mechanical formulation (multi-step) with initial values for the internal plastic variables $\{\boldsymbol{E}^\mathrm{p}, \alpha\}$ set to zero is performed. This inverse elastoplastic calculation results in the first approximation $\boldsymbol{X}_\mathrm{current}$ of the sought material configuration $\mathcal{B}_0$. Applying afterwards the direct FEM by starting at the current material configuration renders the corresponding spatial configuration $\mathcal{B}_\mathrm{t}$ with coordinates $\boldsymbol{x}_\mathrm{current}$. The fitting accuracy of the so found spatial configuration can be tested by the objective function δ, see Eq. (1).

For the case in which only elastic deformations are occurring, the first direct computation recomputes exactly the desired node positions $\boldsymbol{x}_\mathrm{target}$. Hence, the optimal material configuration is already found, as proposed in [6] for the case of elasticity.

On the contrary, if the inverse computation (multi-step) starting at the target configuration computes plastic deformations, the testing after the first subsequent direct computation does not satisfy the given tolerance limit in general. The optimal material configuration is therefore not found in the first iteration loop as in the case of elasticity. This becomes clear by considering that the first direct computation for testing the fitting accuracy starts at the current material configuration with the plastic variables reset to zero. As a consequence, the plastic deformations obtained by the first direct computation cannot equal those of the first inverse computation.

Due to that the form finding algorithm exploits a result, which was already mentioned in Sec. 1. Germain and Steinmann [11] showed that for the case where the plastic variables $\{\boldsymbol{E}^\mathrm{p}, \alpha\}$ are given, the material configuration is recalculated exactly by the inverse computation. Therefore, one starts again with the desired configuration $\boldsymbol{x}_\mathrm{target}$, see Fig. 2. By starting a new inverse computation the plastic variables $\{\boldsymbol{E}^\mathrm{p}, \alpha\}_\mathrm{current}$ of the previous direct calculation are inserted when formulating the inverse weak form. With this update of the plastic variables, a better approximation to the optimal material configuration is found after resolving the inverse procedure. A subsequent direct computation results in a reduced objective function δ. This recursive approach is performed in the spirit of a fixed-point iteration with respect to the plastic variables $\{\boldsymbol{E}^\mathrm{p}, \alpha\}_\mathrm{current}$ until the error measured by δ decreases below a certain tolerance. If this is the case, the optimum blank design to the forming process is found.

The inverse computations for updating the material coordinates $\boldsymbol{X}_\mathrm{current}$ are performed within only one step. The problem remains elastic because the plastic strains are given, see [1]. Therefore, the inverse one-step solutions are faster than the very first multistep computation in the form finding algorithm, see Fig. 2.

4. Numerical examples

The algorithm for inverse form finding is demonstrated by two examples. Regarding the adaptability to different metal forming processes, a displacement-controlled computation can be seen as the simplest approximation to a metal forming with contact, e.g., stamping or expanding a workpiece. On the other hand, a force controlled computation appears, e.g., in the case of forming due to internal pressure. Thus, the first example is carried out by displacement control, while the second example is computed by force control.

The same target configuration of the deformed workpiece is used in both examples, see Fig. 3. Its deformed shape has an external radius of 20 mm, an internal radius of 10 mm and a thickness of 2 mm.

The boundary constraints are identical for both examples. The displacements of the bottom nodes are set to zero in vertical direction. The perpendicular symmetry planes in horizontal direction are clamped by setting the displacements on the one hand in $\boldsymbol{x}_1$-direction and on the other hand in $\boldsymbol{x}_2$-direction to zero. The applied constraints are additionally illustrated in Fig. 3 (red).

The material data used in both examples, see Table 4, are in accordance with a DC04-steel. As proposed in [20], DC04 is a mild deep drawing steel, which is frequently used in the sheet metal

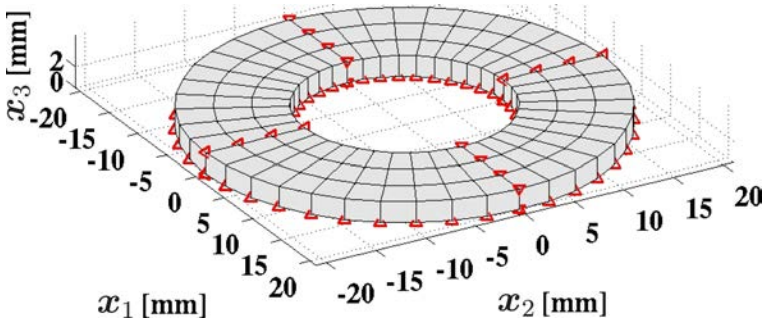

Fig. 3. Boundary constraints (red) for both examples depicted in the target spatial configuration.

forming industry and is characterized by a low yield stress as well as a large fracture strain. To model hardening, a nonlinear Hockett-Sherby function is used, see Table 4. The orthotropic Hill yield criterion, described in Subsec. 2.2, was utilized in both examples to demonstrate that the inverse form finding algorithm, see Sec. 3, is also applicable to anisotropic plasticity.

Table 4. Material parameters for both examples.

Elastic constants			
E-module	E	$= 210000$	[MPa]
Poisson's ratio	ν	$= 0.33$	[-]
Hardening: Hockett-Sherby function			
hardening function	$y(\alpha) = y_\infty - [y_\infty - y_0] \cdot \mathrm{e}^{A\alpha^B}$		
inifinite yield stress	y_∞	$= 680$	[MPa]
initial yield stress	y_0	$= 180$	[MPa]
parameter	A	$= -2.1771$	[-]
parameter	B	$= 0.667$	[-]

4.1. Example 1: enlarging the internal radius by displacement control

The first example is carried out under displacement control by enlarging the internal radius from 6 mm to 10 mm. The total displacements are applied in 10 equidistant load steps. The yield stresses y_{ij} in each direction are, in relation to the initial reference yield stress y_0, set to

$$\begin{aligned} y_{11} = y_{22} = \frac{1}{2} y_0, \qquad y_{33} = y_0, \\ y_{12} = y_{23} = y_{13} = \sqrt{3} y_0. \end{aligned} \tag{19}$$

The anisotropy ratios of y_{11} and y_{22} to y_0 are therefore reduced in comparison to the isotropic von Mises plasticity, see Eq. (19). Consequently, the plastic flow in {1,1}- and {2,2}-direction starts at an earlier stage. As a consequence an orthotropic plastic behavior can be observed and the optimal material configuration turns out to have a square-like form, see Fig. 4.

At the first iteration an error value of $2.3 \cdot 10^{-1}$ mm^2 was obtained, see Table 5. The form finding algorithm, presented in the previous section, reduces this value monotonically. Only six iterations are needed until the error in the objective function decreases below the tolerance of $1 \cdot 10^{-9}$ mm^2.

Table 5 demonstrates an almost linear rate of convergence for finding the optimum blank design. The maximum equivalent plastic strain in this example has a value of 54.55%, see Fig. 4.

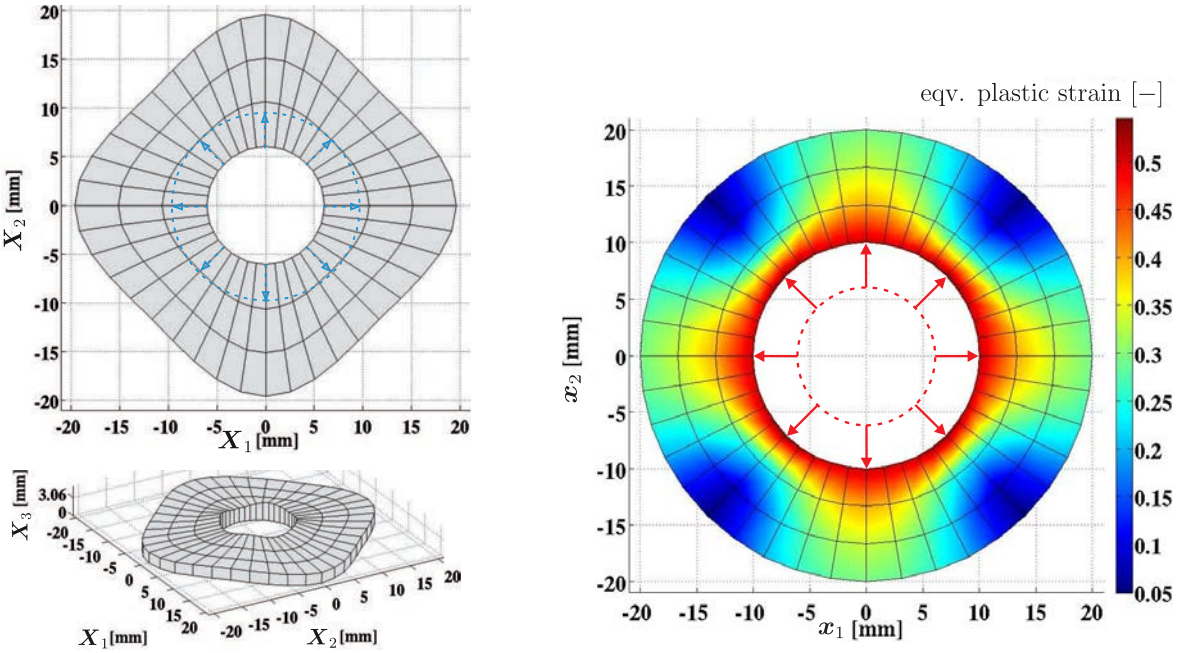

Fig. 4. Example 1: the found optimal material configuration ($\boldsymbol{X}_{\text{Opt}} = \boldsymbol{X}_{\text{current}}$) of the workpiece (left). The target spatial configuration of the workpiece ($\boldsymbol{x}_{\text{current}} = \boldsymbol{x}_{\text{target}}$) after the final direct simulation based on the determined optimal material configuration (right).

Table 5. Convergence rate (Example 1).

Iteration	Error δ [mm^2]
1	$2.3031 \cdot 10^{-1}$
2	$3.2264 \cdot 10^{-3}$
3	$5.1591 \cdot 10^{-5}$
4	$5.5502 \cdot 10^{-7}$
5	$4.2022 \cdot 10^{-9}$
6	$7.0821 \cdot 10^{-11}$

4.2. Example 2: enlarging the internal radius by force control

In the second example, the desired workpiece is loaded by forces of magnitude 800 N applied at each node of the internal radius. The direction of the load application is chosen normal to the surface of the internal radius in the spatial target configuration. In this example, the total forces are applied in 20 equidistant load steps. The initial yield stresses in the orthotropy directions are set to

$$y_{11} = y_{22} = \frac{3}{2} y_0, \qquad y_{33} = y_0,$$
$$y_{12} = y_{23} = y_{13} = \sqrt{3} y_0. \tag{20}$$

By enlarging the anisotropy ratios of y_{11} and y_{22} in comparison to the isotropic von Mises plasticity, see Eq. (20), the plastic flow in {1,1}- and {2,2}-direction in this case starts at later stage. Due to the orthotropic plastic behavior the optimal material configuration turns out again to have a square-like form. In contrast to the displacement controlled example, the inner hole of the optimal material shape also has a square-like form. Additionally, the top nodes of the inner hole have the same height in contrast to the wavy surface in the previous example, see Figs. 4 and 5.

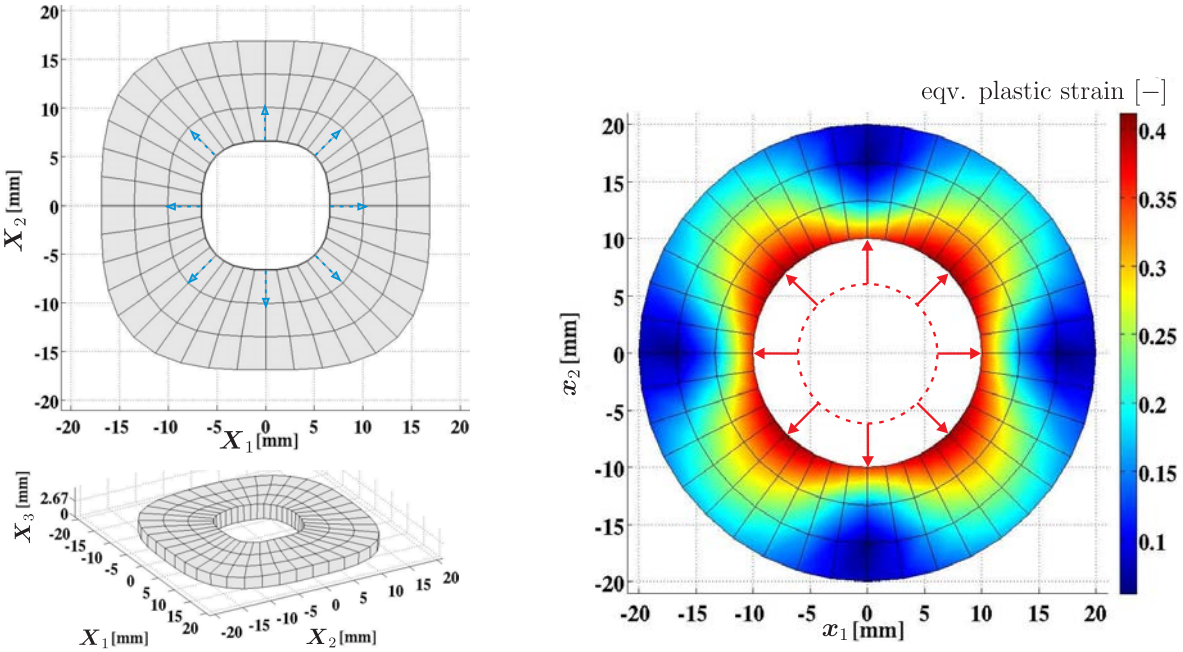

Fig. 5. Example 2: the found optimal material configuration ($\boldsymbol{X}_{\text{Opt}} = \boldsymbol{X}_{\text{current}}$) of the workpiece (left). The target spatial configuration of the workpiece ($\boldsymbol{x}_{\text{current}} = \boldsymbol{x}_{\text{target}}$) after the final direct simulation based on the determined optimal material configuration (right).

For the first iteration, the error value is equal to $1.18 \cdot 10^1$ mm^2, see Table 6, which is higher in comparison to the previous example. This is caused by the fact that the nodes of the internal radius where the largest plastic strains appear are not displacement-fixed as in the previous case. However, the form finding algorithm decreases the error value monotonically. Again only six iterations are needed until the value of the objective function decreases below the tolerance of $1 \cdot 10^{-9}$ mm^2.

Table 6. Convergence rate (Example 2).

Iteration	Error δ [mm^2]
1	$1.1773 \cdot 10^{1}$
2	$4.4566 \cdot 10^{-3}$
3	$1.3130 \cdot 10^{-4}$
4	$1.8014 \cdot 10^{-6}$
5	$3.7573 \cdot 10^{-7}$
6	$9.1649 \cdot 10^{-10}$

Table 6 demonstrates again a nearly linear rate of convergence for finding the optimum blank design. The maximum equivalent plastic strain in this case has a value of 41.21%. The plastic strains appear, due to enlarging the anisotropy ratios of y_{11} and y_{22}, rotated by 45° as compared to the first example, see Fig. 5.

5. Conclusion

By extending the constitutive modeling to anisotropic plasticity, the recursive strategy proposed by [1] is also applicable for inelastic anisotropic inverse form finding problems. The ability of applying force and displacement controlled loads shows, that this method can be used for a couple of applications in metal forming. This was demonstrated by computing two optimal material configurations of a workpiece subject to specific forming processes. The anisotropic Hill yield criterion, which is frequently used in metal forming, was employed for both examples. In both cases, the op-

timum blank design was found with an almost linear convergence rate, even for strong anisotropy ratios and large plastic strains. The problem of mesh distortions, often occurring in sensitivity analysis, does not occur in this proposed recursive strategy. A great advantage of this algorithm is its low computational costs in comparison to other form finding methods. An additional benefit is that the first elastoplastic inverse step results already in a good approximation of the optimum blank design. In case of elasticity, the optimum material configuration is even found within the first iteration.

Acknowledgement

This work is part of the collaborative research project *Manufacturing of complex functional components with variants by using a new metal forming process – Sheet-bulk metal forming* (SFB/TR73: http://www.tr-73.de).

References

[1] S. Germain, P. Landkammer, P. Steinmann. On a recursive formulation for solving inverse form finding problems in isotropic elastoplasticity. *Advanced Modeling and Simulation in Engineering Sciences*, submitted in 2013.

[2] S. Germain, P. Steinmann. Shape optimization for anisotropic elastoplasticity in logarithmic strain space. *Proceedings of the XIth Int. Conf. on Computational Plasticity*, ISBN: 978-84-89925-73-1, 1479–1490, 2011.

[3] S. Acharjee, N. Zabaras. The continuum sensitivity method for computational design of three-dimensional deformation processes. *Comput. Methods Appl. Mech. Eng.*, **195:** 6822–6842, 2006.

[4] S. Germain, P. Steinmann. On a recursive algorithm for avoiding mesh distortion in inverse form finding. *Journal of the Serbian Society for Computational Mechanics (JSSM)*, **6**(1): 216–234, 2012

[5] M. Scherer, R. Denzer, P. Steinmann. A fictious energy approach for shape optimization. *Int. J. Numer. Meth. Eng.*, **82**: 269–302, 2010.

[6] S. Govindjee, P.A. Mihalic. Computational methods for inverse ?nite elastostatics. *Comput. Methods Appl. Mech. Eng.*, **136**: 47–57, 1996.

[7] S. Govindjee, P.A. Mihalic. Finite deformation inverse design modeling with temperature changes, axis-symmetry and anisotropy. UCB/SEMM-1999/01, University of California, Berkeley, 1999.

[8] S. Germain, M. Scherer, P. Steinmann. On inverse form finding for anisotropic hyperelasticity in the logarithmic strain space. *International Journal of Structural Changes in Solids*, **2**(2): 1–16, 2011.

[9] S. Germain, P. Steinmann. A comparison between inverse form finding and shape optimization methods for anisotropic hyperelasticity in the logarithmic strain space. *Proc. Appl. Math. Mech. (PAMM)*, **11**: 367–368, 2011.

[10] A. Ask, R. Denzer, A. Menzel, M. Ristinmaa. Inverse-motion-based form finding for quasi- incompressible ?nite electroelasticity. *Int. J. Numer. Meth. Eng.*, **94**(6): 554–572, 2013.

[11] S. Germain, P. Steinmann. On inverse form ?nding for anisotropic elastoplastic materials. *AIP Conference Proceedings*, **1353**: 1169–1174, 2011.

[12] C. Miehe, N. Apel, M. Lambrecht. Anisotropic additive plasticity in the logarithmic strain space, modular kinematic formulation and implementation based on incremental minimization principles for standard materials. *Comput. Methods Appl. Mech. Eng.*, **191**: 5385–5425, 2002.

[13] N. Apel. *Approaches to the description of anisotropic material behavior at finite elastic and plastic deformations – theory and numerics*, PhD dissertation, University of Stuttgart, 2004.

[14] C. Miehe, M. Lambrecht. Algorithms for computation of stresses and elasticity moduli in terms of the Seth-Hill's family of generalized strain tensors. *Comput. Methods Appl. Mech. Eng.*, **17**: 337–353, 2001.

[15] R. Mahnken. Anisotropy in geometrically non-linear elasticity with generalized Seth-Hill strain tensors projected to invariant subspaces. *Comm. Num. Meth. Eng.*, **21**: 405–418, 2005.

[16] C. Miehe, N. Apel. Anisotropic elastoplastic analysis of shells at large strains. A comparison of multiplicative and additive approaches to enhanced finite element design and constitutive modelling. *Int. J. Numer. Meth. Eng.*, **61**: 2067–2113, 2004.

[17] R. Hill. *The mathematical theory of plasticity* (reprint), Clarendon Press, Oxford, 1989

[18] R. De Borst, P.H. Feenstra. Studies in anisotropic plasticity with reference to the Hill criterion. *Int. J. Numer. Meth. Eng.*, **29**: 315–336, 1990.

[19] S. Germain. *On inverse form finding for anisotropic materials in the logarithmic strain space.* PhD dissertation, University of Erlangen, 2013.

[20] E. Lehmann, S. Schmaltz, S. Germain, D. Fassmann, C. Weber, S. Loehnert, M. Schaper, F.-W. Bach, P. Steinmann, K. Willner, P. Wriggers. Material model identification for DC04 based on the numerical modelling of the polycrystalline microstructure and experimental data. *Key Engineering Materials*, **504–506**: 993–998, 2012.